ACS OMEGA

http://pubs.acs.org/journal/acsodf

Article

Fabrication of Robust and Stable N-Doped ZnO/Single-Walled Carbon Nanotubes: Characterization, Photocatalytic Application, Kinetics, Degradation Products, and Toxicity Analysis

Md. Abu Hanif,* Young-Soon Kim, Jeasmin Akter, Hong Gun Kim, and Lee Ku Kwac*

Cite This: *ACS Omega* 2023, 8, 16174–16185

Read Online

ACCESS | Metrics & More | Article Recommendations | Supporting Information

ABSTRACT: The production of effective visible-light (VL) photocatalysts for the elimination of noxious organic pollutants from wastewater has attracted considerable interest owing to increasing awareness worldwide. Despite the large number of photocatalysts reported, the selectivity and activity of photocatalysts still need to be developed. The goal of this research is to eliminate toxic methylene blue (MB) dye from wastewater through a cost-effective photocatalytic process using VL illumination. A novel N-doped ZnO/carbon nanotube (NZO/CNT) nanocomposite was successfully synthesized via a facile cocrystallization method. The structural, morphological, and optical properties of the synthesized nanocomposite were systematically investigated. The as-prepared NZO/CNT composite exhibited remarkable photocatalytic performance (96.58%) within 25 min of VL irradiation. The activity was 92, 52, and 27% greater than that of photolysis, ZnO, and NZO, respectively, under identical conditions. The enhanced photocatalytic efficiency of NZO/CNT was attributed to the N atom and CNT involvement: N contributes to narrowing the band gap of ZnO, and CNT captures the electrons and maintains the electron flow in the system. The reaction kinetics of MB degradation, catalyst reusability, and stability were also investigated. In addition, the photodegradation products and their toxicity effects in our environment were analyzed using the liquid chromatography–mass spectrometry and ecological structure activity relationships programs, respectively. The findings of the current study demonstrate that the NZO/CNT nanocomposite can be utilized to remove contaminants in an environmentally acceptable manner, thereby providing a new window for practical applications.

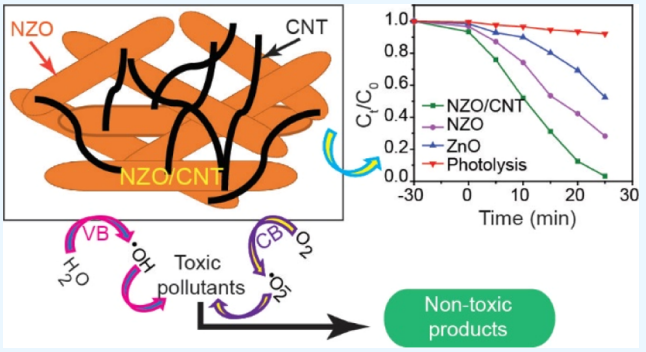

1. INTRODUCTION

The amount of harmful pollutants in the atmosphere has significantly increased as a result of increased industrial activity during the past few decades.[1,2] Environmental contamination is now a major threat to both human health and aquatic life.[3] Organic pollutants present in aquatic ecosystems, such as colorless organic debris antibiotics and colored dyes, are extremely hazardous. Colored dyes are mostly heterocyclic chemical compounds with sulfonic groups and N=N linkages in the structure. Among them, methylene blue (MB), an organic dye, is one of the most frequently employed colorants in different industries.[4] The industry has used dyes extensively, resulting in the production of a significant amount of dye wastewater released into waterbodies without treatment.[3] People who are exposed to MB experience severe health issues, and it severely harms aquatic life.[4] This indicates that dye-containing water must be treated before being released into the environment. However, owing to the complex structural properties of the dye molecules, their degradation is challenging.

Numerous dye treatment techniques have been used to completely mineralize dyes, including photocatalytic degradation, biodegradation, electrolysis, ozonization, ion exchange, reverse osmosis, adsorption, chemical oxidation, and coagulation.[5,6] However, unfortunately, most of these techniques are nondestructive and merely transfer contaminants from one form to another.[7] Among these approaches, the advanced oxidation process by heterogeneous photocatalysis of semiconductors is suitable as a green and sustainable process for converting a variety of inorganic contaminants and organic dyes into environmentally friendly products. In addition, it requires no hazardous, toxic, or environmentally harmful substances and is simple and cost-effective.[3]

Received: January 18, 2023
Accepted: April 18, 2023
Published: April 28, 2023

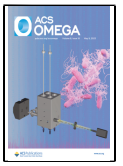

Metal oxide semiconductors have demonstrated decent photocatalytic activity when exposed to visible light (VL) and have been utilized to convert toxic organic dyes into nontoxic forms. Recently, ZnO, CeO_2, In_2O_3, WO_3, and TiO_2 metal oxide nanoparticles have been widely used to degrade contaminants.[8−12] Among them, ZnO semiconductor photocatalysts are preferred as the first choice because of their high quantum efficiency. It also has several unique benefits, including stability, high photocatalytic activity, and low cost.[13−15] However, ZnO semiconductors are ineffective under VL illumination and are only useful when exposed to UV light because of their wide band gap (∼3.37 eV). Thus, when ZnO is used as the catalyst, the amount of sunlight that can be utilized is limited for the photocatalytic process, and only 3−5% of the UV light that reaches the earth is useful. In addition, quick photogenerated electron−hole (e^-−h^+) pair recombination of ZnO must also be resolved for its application.[13,16] Therefore, reducing the band gap to enable absorption in the visible range and preventing photogenerated e^-−h^+ pair recombination have been popular topics among researchers in recent years.

Several approaches have been developed for improving the photocatalytic activity of ZnO. Metals and nonmetals have been incorporated into ZnO to change the light absorption in the VL range or increase the catalytic activity. Nonmetal ion-doped ZnO has recently gained considerable interest as a photocatalyst because of its photogenerated charge carrier transfer ability and increased light absorption.[13,17] Nitrogen (N) appears to be a promising dopant among nonmetal elements because of its similar size to oxygen (O) and lower electronegativity to O.[7,18] Different methods have been developed to synthesize N-doped ZnO (NZO), including high-energy milling, pulsed laser deposition, spray pyrolysis, reactive magnetron sputtering, chemical vapor deposition (CVD), wet chemical processes, hydrothermal processes, and the sol−gel process.[18−25] Another approach is to enhance the photocatalytic performance of ZnO coupled with carbon nanotubes (CNTs). ZnO nanoparticles have been successfully bonded to the surfaces of CNTs in several studies. Owing to their distinctive mesoporous surfaces and strong chemical stability, CNTs offer substantial electrical and conductive properties that allow for the physical adsorption of contaminants.[26,27] CNTs have several exceptional benefits, including excellent electrical and conductive capabilities, robust adsorptive capacity, and superior chemical durability. In addition, CNTs have a high electron storage capacity, which can accept the photogenerated electrons of ZnO at the ZnO−CNT heterojunction interface, thus enhancing photocatalytic performance.[16]

Herein, we propose a novel NZO/CNT nanocomposite, which is synthesized via a simple approach and used to remove organic dyes from wastewater. Three distinct components (N, ZnO, and CNTs) were effectively incorporated into the NZO/CNT composites. The photocatalytic activity of the composites was excellent under VL because of the advantages from each component. First, the incorporation of N into ZnO (NZO) reduces its band gap, which enhances its catalytic efficiency. Subsequently, NZO was combined with CNTs (NZO/CNT composite) to increase its activity. The NZO/CNT composite demonstrated enhanced catalytic efficiency under VL. A heterojunction was created between NZO and CNTs when they were combined. Therefore, a decrease in the recombination of e^-−h^+ pairs leads to an increase in the electron transport rate, which improves the photocatalytic efficiency. The photocatalytic efficiency of NZO/CNT for MB deterioration was higher than those of ZnO and NZO. The photocatalytic effectiveness of NZO/CNT was not significantly affected after five successive cycles, suggesting its exceptional stability and reusability. A deterioration mechanism of the nanocomposite was proposed. In addition, photocatalytic degradation products and their toxicities were investigated. To the best of our knowledge, a similar approach for preparing NZO/CNT composites and their present applications has not been reported to date.

2. MATERIALS AND METHODS

2.1. Materials. Zinc acetate dihydrate [$Zn(CH_3COOH)_2 \cdot 2H_2O$, 99.0%], single-walled CNT (>90%), ethyl alcohol (C_2H_5OH, 99.5%), sodium hydroxide (NaOH, 97%), hydrochloric acid (HCl, 37%), formic acid (HCOOH, 98−100%), and acetonitrile (CH_3CN, ≥99.5%) were obtained from Sigma-Aldrich (St. Louis, MO, USA). Ammonia gas (NH_3, 99.99%) was obtained from Hankok Special Gases Co. (Korea).

2.2. Synthesis of N-Doped ZnO/CNT. NZO/CNTs were fabricated using a simple cocrystallization technique. First, ZnO and NZO were prepared via simple and affordable methods.[28] Subsequently, NZO was used to manufacture NZO/CNT products. ZnO was produced using a modified thermal technique. A quartz crucible was filled with 3 g of zinc acetate dihydrate, and it was covered with a lid in a conventional experiment to produce ZnO. An oxygen-free copper gasket was used to seal the crucible in a stainless-steel chamber (SUS314; length: 60 mm and diameter: 35 mm). A furnace (KSL-1100X-S-UL-LD, USA) was used to heat the compartment for 8 h at 400 °C at a 5 °C min^{-1} heat-up rate. The furnace was allowed to cool to room temperature without being touched after thermolysis to produce ZnO homogeneously and consistently. Subsequently, N was doped onto the already produced ZnO using CVD. In this experiment, 500 sccm each of NH_3 and Ar gases was applied to the freshly synthesized ZnO for 1.4 h at 500 °C. The NZO powder was stored in a sealed bottle for later use. Finally, 0.0250 g of CNTs was dispersed in 200 mL of ethanol for 60 min at room temperature (25 °C) using ultrasonication. Subsequently, 0.2000 g of NZO was added to the dispersion. The resulting suspension was swirled magnetically for 360 min at 25 °C at a speed of 1000 rpm. The NZO/CNT nanocomposite was then extracted from the sample by allowing it to rest for 360 min. It was then separated using filter paper. The specimen was dried at 60 °C overnight after being cleaned with distilled water and ethanol, and it was then placed in an airtight vial for future use.

2.3. Characterization. X-ray diffraction (XRD, PANalytical, X'Pert PRO, Netherlands) was used to analyze the structural features of the investigated compounds. Cu Kα radiation (λ = 1.5406 Å) was used to record the XRD patterns. The chemical composition, binding energy, and oxidation state of the NZO/CNT composite were analyzed using a Thermo Fisher Scientific NEXSA X-ray photoelectron spectroscopy (XPS) system. Field-emission scanning electron microscopy (FE-SEM; SU8230, Hitachi, Japan) was used to investigate the morphological features. Energy-dispersive X-ray spectroscopy (EDS) was used to examine the elemental composition using an apparatus mounted on a field-emission scanning electron microscope. Transmission electron microscopy (TEM) and high-resolution TEM (HR-TEM, JEM-2200FS, Japan) were

https://doi.org/10.1021/acsomega.3c00370
ACS Omega 2023, 8, 16174−16185

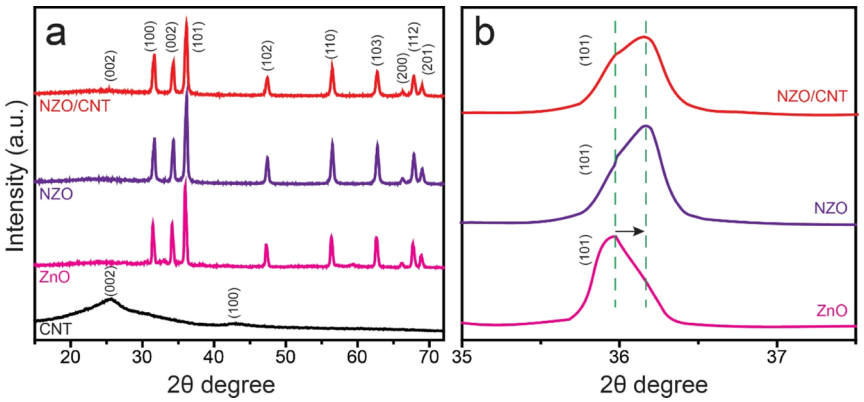

Figure 1. XRD patterns of the (a) CNT, ZnO, NZO, and NZO/CNT composites and (b) magnified scale of the (101) plane for ZnO, NZO, and NZO/CNT composites.

used to study the morphology of the product. UV−vis spectrophotometry was used to investigate the optical characteristics of the nanocomposites (PerkinElmer Lambda 25, Ayer Rajah, Singapore). The photoluminescence (PL) emission spectra (FP-6500, Jasco) were recorded at room temperature. Liquid chromatography−mass spectrometry (LC−MS) data were used to inspect the MB photodegradation byproducts (Agilent 6410 B; Wilmington, USA). Using an electrospray ionization (ESI) interface, ions were produced in ionization mode. At a source temperature of 380 °C and a voltage of +3000 V, ESI was performed. The cone voltage, capillary voltage, and source offset were set to 30, 3, and 30 V, respectively. The nebulizer pressure was adjusted to 15 bar, while the gas flows for desolvation and the cone were adjusted to 650 and 150 L h^{-1}, respectively. The analytes were separated using a mobile phase that contained 0.1% formic acid in distilled water (buffer A) and 0.1% formic acid in acetonitrile (buffer B), which was injected into the ESI chamber at a flow rate of 0.5 mL min^{-1} for 20 min. Each syringe had a volume of 5 L. The interface heater was set at 300 °C, and the fragmentation potential was fixed at 110 V. The ions were detected using the MS full-scan mode.

2.4. Photocatalytic Experiments. The photocatalytic degradation of MB, as a target pollutant, was used to evaluate the photocatalytic performance of each material. A 300 W xenon lamp was used as the VL source during testing. Additionally, a UV cutoff filter (400 nm) was applied to block UV rays. For the photocatalytic activity assays, a 50 mg NZO/CNT sample was combined with an aqueous MB solution (100 mL, 10 mg L^{-1}). The dye solution and catalyst were then combined in a beaker and ultrasonically heated for 60 min at 25 °C. To reach adsorption−desorption equilibrium between the catalyst surface and dissolved MB bodies, the mixture was left in the dark for 30 min. The degradation process was then performed by placing the solution under VL while continuously swirling it. The reduction in the MB concentration was tracked by measuring the absorbance of the solution at 200−750 nm using UV−vis spectrophotometry at regular intervals. An identical volume of solution (2 mL) was collected for each measurement. The typical absorption wavelength of MB (664 nm) was also monitored. To compare the activity of the as-prepared NZO/CNT photocatalyst, three series of tests were performed: photolysis (using only the dye solution and no photocatalyst), ZnO, and NZO. All the experiments were conducted under similar conditions. The recyclability of NZO/CNT was assessed using an identical process for each set. This was accomplished by gathering the precipitated sample (after centrifugation) and repeatedly rinsing it with distilled water. The specimen was subsequently dried in a preheated furnace at 100 °C for approximately 5 h to evaluate the effectiveness of its recycling. The following cycle of the photocatalytic reaction employed a dry sample as the starting point.

3. RESULTS AND DISCUSSION

3.1. Structural Investigation. The crystal structure, phase, purity, and crystallite size of the CNT, ZnO, NZO, and NZO/CNT were investigated using XRD. Figure 1 shows the XRD patterns of all the examined samples. Figure 1a displays the two characteristic peaks of CNT at 25.62 and 42.77° corresponding to the (002) and (100) planes, respectively. These two peaks are obtained because of the formation of *d*-spacing and disordered carbon.[29] The diffraction peaks of ZnO are centered at 31.43, 34.12, 35.98, 47.29, 56.36, 62.61, 66.18, 67.71, and 68.87° corresponding to the (100), (002), (101), (102), (110), (103), (200), (112), and (201) planes, respectively, with hexagonal wurtzite ZnO structure (JCPDS #36-1451). All XRD peaks of ZnO are observed in the curves of the NZO and NZO/CNT compounds. In addition, the CNT (002) plane peak is also observed in the NZO/CNT composite, confirming the successful deposition of CNT on the NZO material. However, the intensity of the CNT (002) plane peak is very low compared to that of ZnO, and the CNT (100) plane is not visible because of the higher-intensity peak of ZnO. As shown in Figure 1b, after N-doping onto ZnO and combining with CNT, in both cases, the (101) plane is shifted toward higher 2θ values compared to that of ZnO. These outcomes suggest that N is doped into the ZnO matrix and successfully combines with the CNT. The XRD curves reveal no additional peaks, indicating that the synthesized compounds are extremely pure.

The average crystallite sizes of the ZnO, NZO, and NZO/CNT composites (all of the aforementioned planes) were evaluated using Scherrer's equation (eq 1)

$$D = k\lambda/\beta \cos\theta \quad (1)$$

where D is the crystallite size, λ is the X-ray wavelength (0.15406 nm), k is the nondimensional shape factor (0.94), θ is the Bragg angle, and β is the full width at half-maximum. The average D values of the ZnO, NZO, and NZO/CNT composites are 23.96, 21.94, and 20.45 nm, respectively.

Furthermore, to calculate the crystallite sizes of the ZnO, NZO, and NZO/CNT compounds more accurately, we used

https://doi.org/10.1021/acsomega.3c00370
ACS Omega 2023, 8, 16174−16185

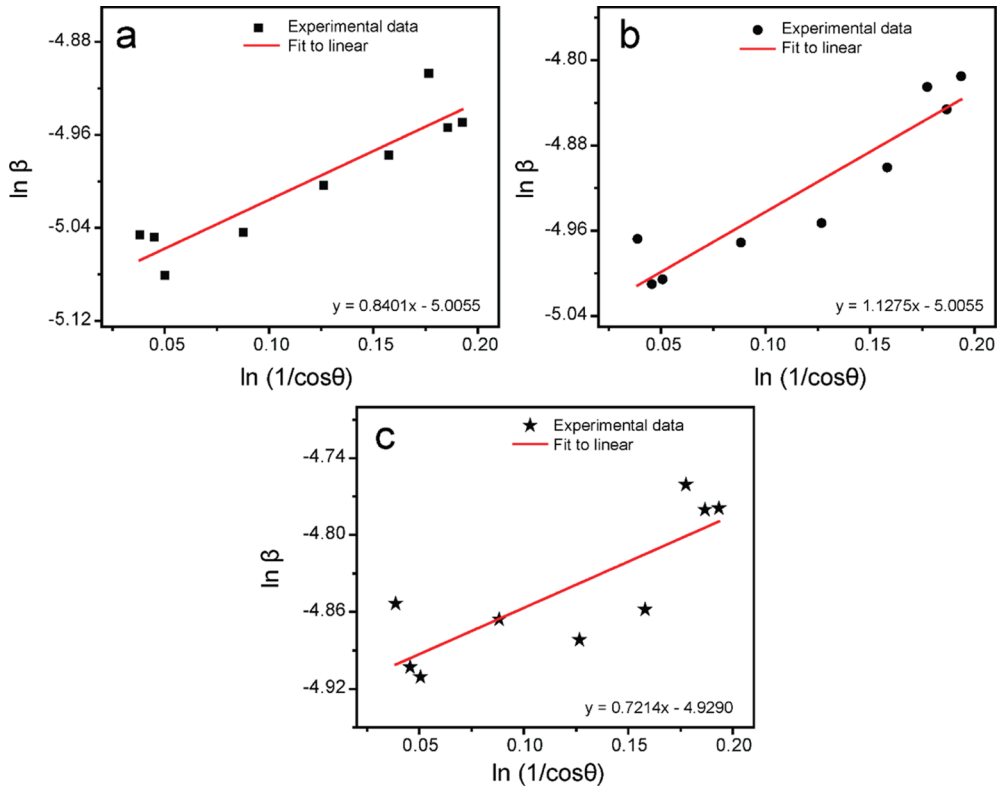

Figure 2. Linear plots of the modified Scherrer equation: (a) ZnO, (b) NZO, and (c) NZO/CNT composites.

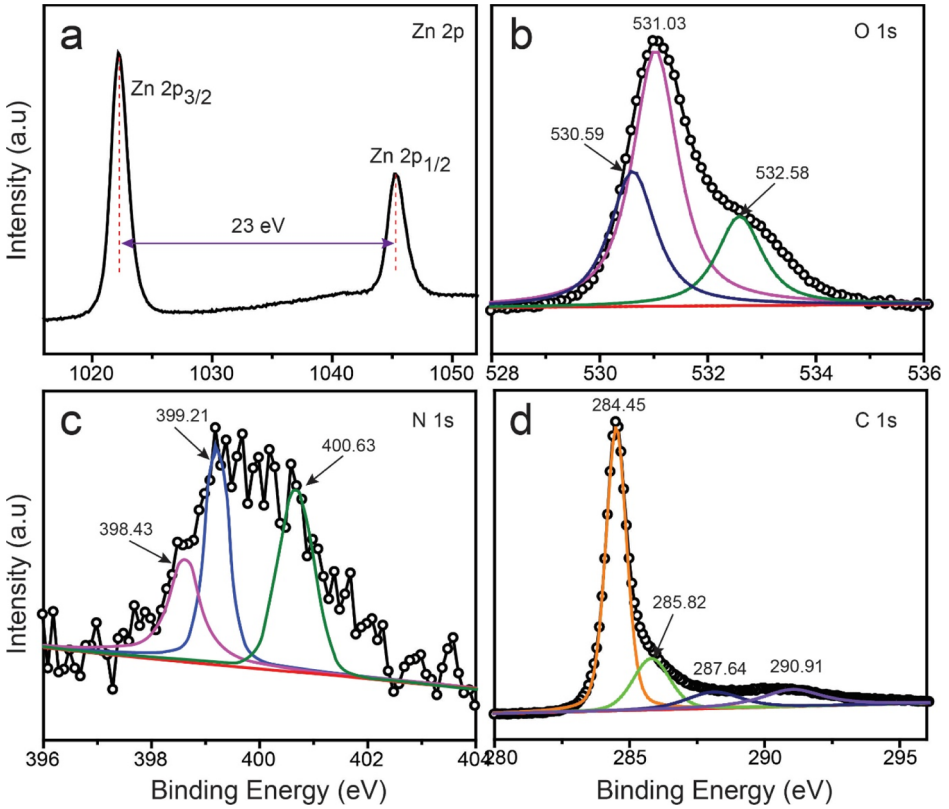

Figure 3. High-resolution XPS spectra of NZO/CNT: (a) Zn 2p, (b) O 1s, (c) N 1s, and (d) C 1s.

the modified Scherrer equation, and the representative curves are shown in Figure 2. The calculated average *D* values of ZnO, NZO, and NZO/CNT are 23.75, 22.71, and 20.02 nm, respectively. Interestingly, the average size and order (ZnO > NZO > NZO/CNT) obtained using both methods are almost identical. The detailed calculation process is as follows:

https://doi.org/10.1021/acsomega.3c00370
ACS Omega 2023, 8, 16174−16185

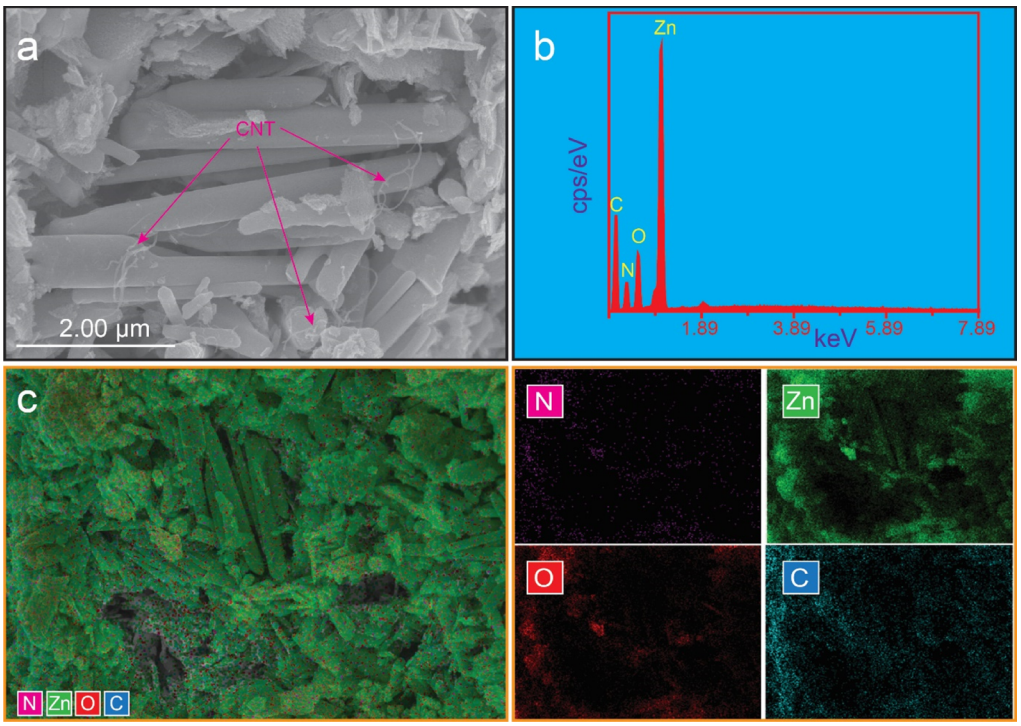

Figure 4. (a) FE-SEM images, (b) EDS spectra, and (c) elemental mapping analysis of NZO/CNT material.

On converting eq 1 into its logarithmic form, we have (eq 2)

$$\ln \beta = \ln[(1/\cos \theta) \times (k\lambda/D)] \quad (2)$$

This equation is known as the modified Scherrer equation. On plotting ln $(1/\cos\theta)$ on the x-axis and ln β on the y-axis, we calculated the crystallite size from the y-intercept value [ln $(k\lambda/D)$].

XPS was used to analyze the elemental composition, oxidation state, and binding energy of the NZO/CNT composites. The XPS survey spectrum of the compound is shown in Figure S1. The wide spectrum indicates that the four representative elements, N, Z, O, and C, are present in the NZO/CNT composite. The NZO/CNT was further systematically studied by collecting its high-resolution XPS spectrum, which included the core-level spectra for Zn 2p, O 1s, N 1s, and C 1s, as shown in Figure 3. The core-level Zn 2p spectrum is shown in Figure 3a. Prominent doublet signals can be seen at the binding energies of 1021.95 and 1044.95 eV, which match the chemical environments of Zn $2p_{3/2}$ and Zn $2p_{1/2}$, respectively. This outcome confirms the formation of the ZnO wurtzite structure and the oxidation state of zinc was +2.[29] The existence of ZnO in the nanocomposite was further confirmed by the fact that the binding energy gap between the Zn $2p_{3/2}$ and Zn $2p_{1/2}$ peaks was 23 eV.[30] The three deconvoluted O 1s peaks are observed at binding energies of 530.59, 531.03, and 532.58 eV (Figure 3b). The lowest energy signal at 530.59 eV is attributed to O^{2-} in the ZnO wurtzite structure. The rest of the two peaks at 531.03 and 532.58 eV correspond to surface-adsorbed H_2O/O_2 from air and oxygen vacancies/defects, respectively.[2] The N 1s curve is deconvoluted into three peaks at binding energies at 398.43, 399.21, and 400.63 eV (Figure 3c). The lowest binding energy peak, located at 398.43 eV, is linked to the O−Zn−N bond.[31] This indicates that N dopants combine at O sites in ZnO nanorods in a substitutional manner.[31] The high-intensity peak at 399.21 eV is ascribed to the N−N and N−C bonds.[18] The binding energy centered at 400.63 eV is responsible for the attachment of doped N to carbon atoms in the CNT. Figure 3d shows the core-level spectrum of C 1s, which is deconvoluted into four peaks at 284.45, 285.82, 287.64, and 290.91 eV. The most intense peak at 384.45 eV originates from sp^2-hybridized graphitic carbon (C═C). The peak at 285.82 eV suggests that there are some defects present in the form of C−C carbon. The other two peaks at 287.64 and 290.91 eV are attributed to −C═O and $\pi-\pi^*$, respectively.[18,32]

3.2. Morphological Investigation. Characteristic FE-SEM images of the NZO/CNT nanocomposite are shown in Figure 4. FE-SEM images of ZnO and NZO are shown in Figure S2. There are two different morphological patterns for these ZnO nanoparticles: one is aggregated almost spherically, whereas the other is rod-shaped (Figure S2a). The formation of aggregated nanoparticles with a roughly spherical shape may have been caused by the accumulation of small particles. The majority of the particles have a rod-like morphology, with an average diameter and length of approximately 450 nm and 3.3 μm, respectively. These rod-shaped ZnO nanoparticles exhibit a wurtzite hexagonal structure.[33] The results (the hexagonal wurtzite assembly) agreed with those of XRD. An FE-SEM image of the NZO nanoparticles is shown in Figure S2b. The shape of the particles is not changed by the addition of N to ZnO, but their sizes vary. The average diameter and length of the particles are roughly 212 nm and 2.1 mm, respectively. These results show that the axial development of ZnO was reduced as a result of the N doping. A similar result was observed when Mn was doped onto the ZnO nanorods.[34] This research proved that the morphology of the particles was unaffected by the doping atom. However, the morphological shape was similar after constructing the composite with CNTs (Figure 4a). A large number of NZO nanorods are observed around each CNT. Magenta arrows were used to easily identify certain CNTs. The NZO nanorods are observed in a regular orientation everywhere in the CNTs. The distance between

https://doi.org/10.1021/acsomega.3c00370
ACS Omega 2023, 8, 16174−16185

CNTs can be observed between the succeeding clusters of NZO. In contrast to the nanorod clusters that are more densely packed when the CNTs are closer to one another, the CNTs are scattered in other locations.

The purity and elemental composition of the as-prepared NZO/CNT were confirmed by EDS. Figure 4b shows the representative EDS spectrum. The sample contains N, Zn, O, and C. These results are consistent with the results of XPS. These results further demonstrated that the NZO/CNT nanocomposite was successfully formed. Furthermore, the absence of additional peaks in the EDS spectrum indicates that the NZO/CNT was free from impurities. Figure S2c,d shows the EDS spectra of ZnO and NZO, respectively. The EDS spectrum of ZnO confirms that only Zn and O are present. In contrast, the NZO material contains three elements: N, Zn, and O.

Furthermore, FE-SEM elemental mapping was employed to inspect the elemental distribution of the NZO/CNT, as shown in Figure 4c. The findings indicated that N, Zn, O, and C were homogeneously distributed throughout the structure.

TEM and HR-TEM were used to analyze the intimate interaction between NZO and the CNTs in the NZO/CNT composite, as shown in Figure 5a,b, respectively. It can be

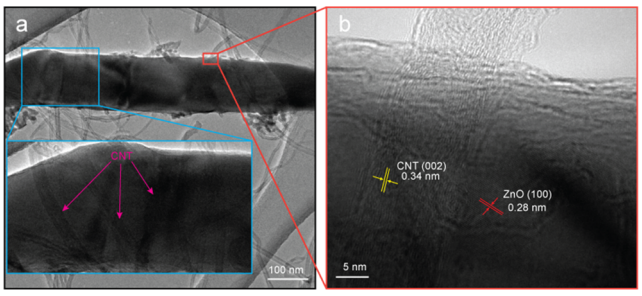

Figure 5. (a) TEM and (b) HR-TEM micrographs of the NZO/CNT composite.

clearly seen that NZO and CNT closely interact with each other. The NZO particles have flat surfaces and are rod-shaped, as observed in the TEM micrographs, which is also confirmed by the FE-SEM observations. Furthermore, HR-TEM was used to study the closeness between NZO and the CNT (Figure 5b). The extremely thin CNTs can be seen as imprints or patterns on the NZO surface in the HR-TEM images. The (100) lattice plane of the NZO hexagonal wurtzite structure is confirmed by measuring the interplanar spacing of ZnO at 0.28 nm. Based on the carbon (002) plane, the lattice spacing for CNTs is calculated to be 0.34 nm. These photographs unequivocally demonstrate that NZO encloses the CNTs. Additionally, this observation provides evidence that an NZO−CNT heterojunction formed between CNT and NZO. Such heterojunction creation might encourage the exchange of charge carriers between the photoinduced elements and boost their photocatalytic activity.

3.3. Optical Investigation. The practical implementation of semiconductor compounds as photocatalysts significantly depends on their optical characteristics. UV−vis spectroscopy data were collected to investigate the optical properties of the compounds. Figure 6 shows the UV−vis spectra of the samples. The maximum absorbance peaks are detected at 267, 368, 373, and 378 nm for the pristine CNT, ZnO, NZO, and NZO/CNT, respectively. It is noteworthy that the absorbance peak observed in the spectrum of ZnO shifts to longer wavelengths in the spectra of the NZO compound. This redshift proves that a new energy level is added to the band structure of ZnO through direct interaction with the doped N. The NZO/CNT nanocomposite exhibits a maximum wavelength shift toward the visible range. Therefore, when the nanocomposite is utilized as a photocatalyst, this redshift enhances light absorption compared to other materials and subsequently contributes to the superior photocatalytic effect. Electron transport to CNTs may be accelerated, and the rate of e^-−h^+ pair recombination may decrease during photoexcitation.

The optical band gap energy (E_g) of the compounds was determined using Tauc plots and the accompanying UV−vis absorbance data. The Tauc plots of CNT, ZnO, NZO, and NZO/CNT are shown in the insets of Figure 6a−d, respectively. The intercept of the energy axis was calculated by extrapolating the graph of $(\alpha h\nu)^2$ vs E, and the intercept is denoted by E_g where $(\alpha h\nu)^2$ equals 0. The measured E_g values of the CNT, ZnO, NZO, and NZO/CNT were 3.46, 2.82, 2.76, and 2.07 eV, respectively. It is interesting to note that composite construction between NZO and CNTs reduced the E_g value. In general, a reduced E_g value helps boost the photocatalytic action of ZnO-based semiconductor constituents.[29] Among the CNT, ZnO, NZO, and NZO/CNT, NZO/CNT has the lowest E_g value. The addition of N and CNT significantly reduced the band gap of the nanocomposite. The NZO/CNT composites can function in the visible region owing to their lower band gaps. Low-energy light is sufficient to excite valence band (VB) electrons into the conduction band (CB) in the presence of a narrow band gap, which accelerates the photoreaction.

3.4. PL Investigation. The impact of charge carrier recombination on the compounds was assessed using PL analysis. Figure 7 shows the PL spectra of ZnO, NZO, and NZO/CNT at room temperature. All samples show two types of emission peaks in the PL spectra. One peak is observed at 380 nm in the UV region for the recombination of free excitons at the near-band edge of the compounds.

The other comparatively wide emission peak is located near 453−517 nm for the green band owing to oxygen vacancies. Oxygen vacancies are crucial for the production of superoxide ($O_2^{-\bullet}$) and hydroxyl ($OH^\bullet$) radicals. These radicals play a vital role in the deterioration of pollutants from wastewater.[35] In addition, the PL peak intensity and e^-−h^+ pair recombination are intimately correlated; when the peak intensity is lower, the e^-−h^+ pair recombination is lower and vice versa. The PL spectra indicate that the peak intensity decreases in the order ZnO > NZO > NZO/CNT. NZO shows a lower intensity than that of undoped ZnO. This indicates that N doping is essential for preventing the recombination of the photoinduced e^-−h^+ pairs of ZnO. Doping substances produce numerous electron traps that suppress the recombination of e^-−h^+ pairs.[28] Among the three compounds, NZO/CNT possesses the least intensity because it is an electron trapper that helps to reduce the recombination effect.[6] Finally, the electron separation and transfer are enhanced with the decrease in e^-−h^+ pair recombination, improving the photocatalytic effectiveness of the materials. Therefore, the NZO/CNT composite might provide a higher photocatalytic performance than ZnO and NZO.

3.5. Photocatalytic Investigation. The photocatalytic activity of ZnO, NZO, NZO/CNT, and the no catalyst

https://doi.org/10.1021/acsomega.3c00370
ACS Omega 2023, 8, 16174−16185

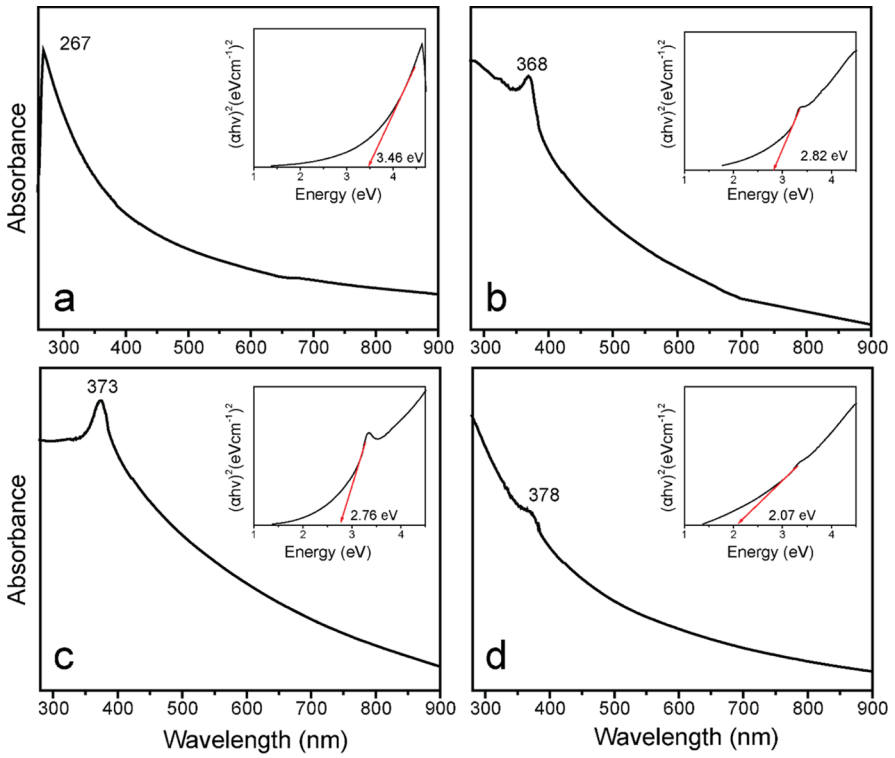

Figure 6. UV−vis absorption spectra of (a) CNT, (b) ZnO, (c) NZO, and (d) NZO/CNT. Each inset represents its corresponding Tauc plots.

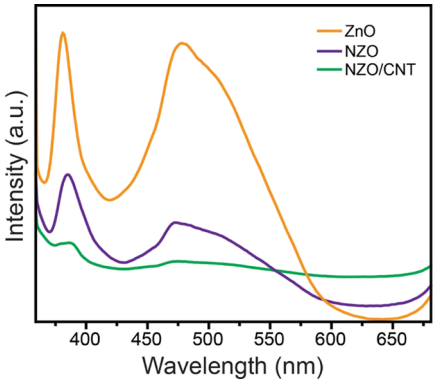

Figure 7. PL spectra of ZnO, NZO, and NZO/CNT composites.

(photolysis) case was investigated for the decomposition of MB dye in the presence of VL illumination for 25 min. The adsorption efficiencies of the samples were investigated under dark conditions. Figure 8a shows the adsorption and photodegradation performance as a function of time. The results show that a negligible adsorption proficiency is observed, and the order increases as follows: photolysis < ZnO < NZO < NZO/CNT. The adsorption activity of NZO/CNT is comparatively higher than that of the other samples owing to the involvement of CNTs in the composite. CNTs are good adsorbents, and their adsorption results mainly from the CNT portion.[36]

The photodegradation efficiency (η) of the samples was measured using the following equation (eq 3)

$$\eta\ (\%) = \frac{C_0 - C_t}{C_0} \times 100 \tag{3}$$

where C_0 and C_t represent the absorbance at 0 and t min, respectively. According to the degradation efficiency of the photolysis experiment, no appreciable amount of MB was degraded in the absence of a catalyst. This rate is accelerated by the use of a catalyst. The activity of NZO was higher than that of ZnO. This implies that N atoms boost the photocatalytic efficiency of ZnO. The NZO/CNT composite demonstrated maximum photocatalytic efficiency (96.58%) within a degradation period of only 25 min. The photodeterioration performance was enhanced in the following order: photolysis (7.42%) < ZnO (46.74%) < NZO (70.87%) < NZO/CNT (96.58%). The NZO/CNT nanocomposite showed 92, 52, and 27% higher photocatalytic activities as compared to photolysis, ZnO, and NZO, respectively. These results indicate that N atoms and CNT are promising materials for improving the performance of ZnO. The lower activity of ZnO is due to its higher band gap, which decreases the production of electrons and holes during photocatalytic reactions. After the incorporation of N atoms into the ZnO matrix, the band gap and PL intensity were reduced (Figures 6 and 7). The lower the bandgap, the higher the photocatalytic activity. However, the activity of NZO is low compared to that of NZO/CNT, which clearly indicates that not only N is responsible for enhancing the proficiency of NZO/CNT but also CNTs play a significant role. The enhancement of the activity of NZO/CNT might be owing to two reasons: (i) N helps to reduce the band gap of ZnO and (ii) CNTs capture the electrons and maintain the flow of electrons. Therefore, the e^-−h^+ pair recombination effect is suppressed and the electron flow is increased, thereby enhancing the photocatalytic activity of NZO/CNT.

To comprehend the photocatalytic performance of the compounds, reaction kinetics were also investigated, and the representative results are shown in Figure 8b. The MB photodegradation rate constant (k) was analyzed using pseudo-first-order kinetics (eq 4)

https://doi.org/10.1021/acsomega.3c00370
ACS Omega 2023, 8, 16174−16185

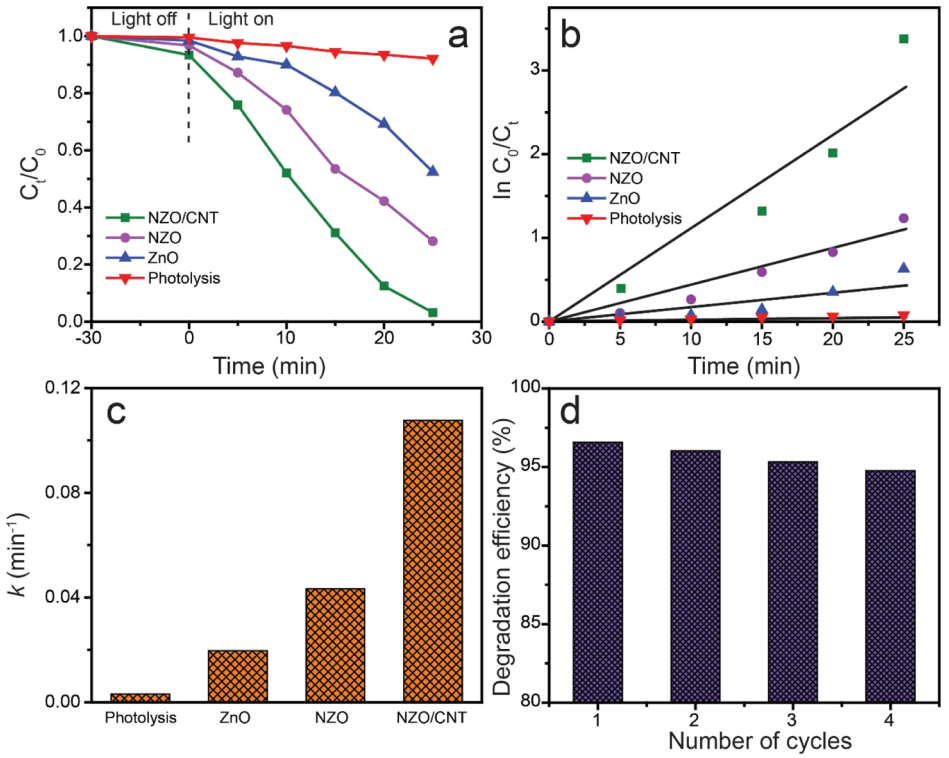

Figure 8. (a) Photodeterioration performance as a function of time, (b) kinetics curves, (c) rate constant of all the inspected samples, and (d) recyclability of the NZO/CNT composite.

$$\ln\left(\frac{C_0}{C_t}\right) = kt \tag{4}$$

where the term "t" corresponds to the irradiation time. The computed k values were 0.0031, 0.0252, 0.0493, and 0.1350 min^{-1} for photolysis, ZnO, NZO, and NZO/CNT, respectively (Figure 8c and Table S1). Among the examined photocatalysts, NZO/CNT showed an enhanced k value (0.1350 min^{-1}), suggesting maximum photocatalytic efficiency. This value was 43.55 times higher than that obtained without a catalyst (photolysis). The reaction in the presence of the NZO/CNT composite achieved a k value that was 5.35 and 2.74 times higher than the reactions in the presence of ZnO and NZO, respectively. These results made it evident that the addition of N and CNT might improve photocatalytic efficiency. Therefore, in comparison to the undoped material, the doping element played a dynamic role in improving the photodegradation proficiency and rate constant. Therefore, compared with those of the separate components, doping and/or the construction of composite materials plays a critical role in improving the rate constant and efficiency. The enhanced electron transport from the VB to the CB may be the cause of this characteristic of doped or composite materials.[3]

The effectiveness of a nanocatalyst, particularly its recyclability and stability, is the key variable to be considered in terms of wastewater treatment cost and preventing the formation of secondary pollutants. From this perspective, MB degradation experiments under VL irradiation were conducted for four consecutive cycles to examine the reusability and stability of the NZO/CNT catalyst. The as-synthesized NZO/CNT material displays 94.77% MB deterioration after four consecutive runs over 25 min, as illustrated in Figure 8d. The small loss of the catalyst during recycling is the cause of the decrease in activity (1.02%). Furthermore, XRD and XPS measurements are performed to evaluate the structural constancy of the NZO/CNT catalyst for up to four cycles (before and after treatment), as shown in Figure S3. After four successive cycles, all significant peaks in both spectra remain after the catalytic reaction. The NZO/CNT photocatalyst exhibits remarkable recyclability and stability. Therefore, it can be applied to the practical implementation of wastewater treatment.

Table S2 compares the photocatalytic degradation capabilities of the as-prepared NZO/CNT photocatalyst with those of previously reported ZnO- or CNT-based composites. These findings demonstrate the superior photocatalytic efficiency of the NZO/CNT catalyst, which quickly reaches a high degradation efficiency.

3.6. Determination of the Point of Zero Charge (pH_{pzc}). Photocatalytic reactions occur on the surface of the catalysts. Therefore, it is crucial to understand the surface characteristics of photocatalysts, particularly their surface charges (SCs). SC is determined by computing the point of zero charge (pH_{PZC}), as shown in Figure 9. The well-known drift method was applied to estimate the pH_{PZC} of NZO/CNT compounds in the pH range of 2−12. The initial pH values (pH_i) of the solutions were adjusted using either NaOH or HCl. After recording the final pH values (pH_f) of the substances, eq 5 was used to compute ΔpH.

$$\Delta pH = pH_f - pH_i \tag{5}$$

The pH_{PZC} value of the NZO/CNT composite was determined by plotting ΔpH vs pH_i, and the results showed that the ΔpH and pH_i values were equal to 6.18. Therefore, the calculated pH_{PZC} value of NZO/CNT was 6.18. The surface of the NZO/CNT nanocomposites has a positive

https://doi.org/10.1021/acsomega.3c00370
ACS Omega 2023, 8, 16174−16185

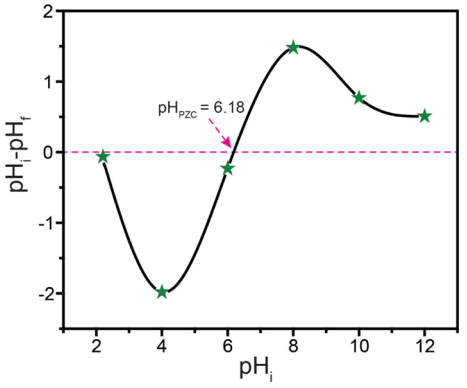

Figure 9. Determination of pH_{PZ} using the NZO/CNT catalyst.

charge at pH levels lower than the pH_{PZC} value (repelling cations), while pH levels upstairs pH_{PZC} favor the formation of a negative charge (attracting cations). Hence, the positively charged MB dye repels electrons owing to cationic nature of MB, and the photodegradation activity is reduced at pH levels below 6.18 (acidic medium). Conversely, the positively charged MB and the catalyst surface interacted strongly when the pH was higher than 6.18 (basic medium) which increased the photodegradation efficiency.

3.7. Proposed Photocatalytic Degradation Mechanism. Figure 10 shows the possible photocatalytic degradation

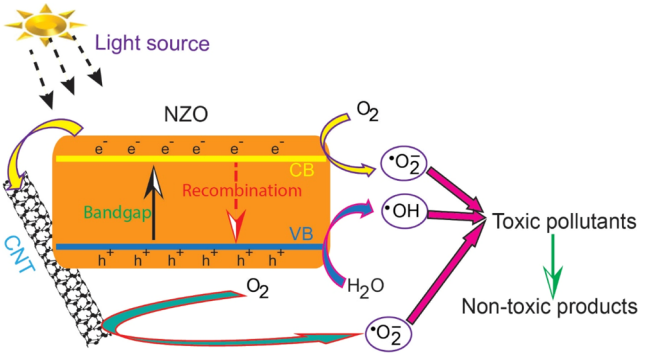

Figure 10. Probable photodegradation mechanism of MB dye using NZO/CNT.

mechanism of the aqueous MB solution in the presence of the NZO/CNT photocatalyst. The photocatalytic reaction was initiated on the surface of the NZO/CNT via the adsorption of MB molecules with the assistance of a light source. After that, the NZO/CNT catalyst was excited, and the photoinduced electrons (e^-) in the CV and holes (h^+) in the VB were produced during VL irradiation. h^+ is held in the VB, whereas e^- is held in the CB. Consequently, e^-–h^+ pairs were created on the catalyst surface. e^- serves as a reducing agent, whereas h^+ serves as an oxidizing agent. $HO^\bullet$ is generated in the VB when h^+ and H_2O interact with each other. Meanwhile, CB produces superoxide radicals ($^\bullet O_2^-$) through a reaction between oxygen molecules and e^-. The $^\bullet O_2^-$ radicals then participate in further reactions, resulting in the production of $HO^\bullet$ radicals. Utilizing single-walled CNT constructions in composite materials not only offers well-defined pathways for electron transport but also ensures a wide range of possibilities for charge-transfer optimization without sacrificing light absorption due to their smaller size compared to multiwalled CNTs and graphene sheets.[37−39] In addition, e^- is simply pushed into CNTs because of the modest Fermi energy of CNTs. CNTs play a vital role as a rapid electron transporter in the nanocomposite because of their one-dimensional structure. Hence, the CNT-based composite may effectively prevent e^-–h^+ pairs recombination and provide more holes to accelerate the decomposition of pollutants due to the electron-transporting and electron-accepting capabilities of CNTs.[40,41] However, it is worth acknowledging that CNTs play a vital role in reducing the recombination effect and enhancing the separation of e^- and h^+ owing to their high electron-storage capacity.[16] CNT may serve as a sink for the photoexcited electrons originating from the NZO compound, thereby producing chemical interactions between NZO and CNT. Consequently, several e^- are transported to the CNT from NZO, which lowers the rate of e^-–h^+ pair recombination, increases the lifetime of e^-–h^+ pairs, and enhances the photocatalytic efficiency of the products.

Below is a summary of the principal chemical reactions during the photocatalytic process (eqs 6–12)

$$\text{NZO/CNT} + h\nu \rightarrow \text{NZO/CNT}\ (e^-_{CB} + h^+_{VB}) \quad (6)$$

$$O_2 + \text{NZO/CNT}\ (e^-_{CB}) \rightarrow \text{NZO/CNT} + {}^\bullet O_2^- \quad (7)$$

$${}^\bullet O_2^- + H^+ \rightarrow {}^\bullet HO_2 \quad (8)$$

$$H_2O + \text{NZO/CNT}\ (h^+_{VB}) \rightarrow \text{NZO/CNT} + {}^\bullet OH + H^+ \quad (9)$$

$${}^\bullet HO_2 + {}^\bullet HO_2 \rightarrow O_2 + H_2O_2 \quad (10)$$

$${}^\bullet O_2^- + H_2O_2 \rightarrow {}^\bullet OH + O_2 + HO^- \quad (11)$$

$$\text{Toxic pollutants} + ({}^\bullet OH, H^+, {}^\bullet O_2^- \rightarrow \text{Nontoxic products} \quad (12)$$

3.8. LC–MS Investigation. MB was remarkably stable under VL illumination when no catalyst was used, but it degraded with the production of a number of intermediate compounds in the presence of the NZO/CNT photocatalyst with VL exposure. The intermediates were analyzed by LC–MS. The degradation process with a catalyst involves the production of photoexcited e^- and h^+ which subsequently produce $OH^\bullet$ and $O_2^{\bullet-}$ radicals. The active species function as degradation agents because of their high reactivity and the degradation of MB. The intermediates formed because degradation was analyzed using LC–MS. The MS data obtained before and after photocatalysis for 25 min of VL irradiation are shown in Figure 11. The existence of MB inside the mixed solutions is confirmed by the stronger signal in Figure 11a at m/z = 284. The distinctive peak of MB (m/z =

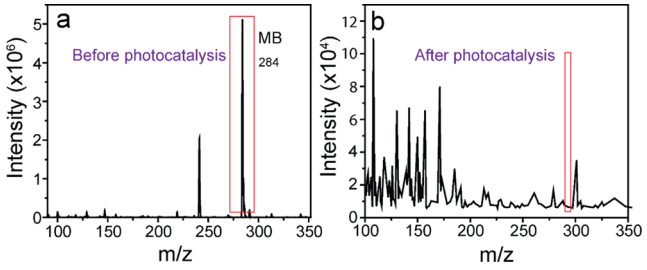

Figure 11. Mass spectra of MB aqueous solution (a) before and (b) after photocatalytic action using the NZO/CNT nanocomposite.

https://doi.org/10.1021/acsomega.3c00370
ACS Omega 2023, 8, 16174−16185

Table 1. Theoretically Calculated Values of Aquatic and Chronic Toxicity of MB Dye and Its Degradation Intermediates

	m/z	Acute toxicity LC/EC$_{50}$ (mg L^{-1})			Chronic toxicity ChV (mg L^{-1})
		Fish	Daphnid	Green	Fish
MB	284	5.79	3.88	5.72	0.688
P1	336	11500	5550	2070	927
P2	301	693	376	232	64.2
P3	279	287	161	115	27.7
P4	267	880	470	271	80
P5	214	10400000	4020000	603000	645000
P6	190	40200000	14500000	1650000	2300000
P7	184	1060	552	287	93.6
P8	171	6210000	2190000	226000	345000
P9	156	6440000	2260000	228000	356000
P10	148	315000	140000	37300	23000
P11	142	480	256	147	43.5
P12	130	17700000	5810000	450000	907000
P13	125	2070	1030	440	173
P14	109	669	347	179	58.8
P15	102	2080	1140	715	194
Toxic		Harmful			Not harmful

284) entirely vanishes, as shown in Figure 11b, and peaks are observed at several new m/z values connected to the intermediate products. Degradation products are proposed based on their m/z values, as shown in Figure S4. First, it was suggested that the main degradation process would involve the center rings by oxidizing the C−S^{+}═C groups and imino groups. Oxidation occurred through hydroxyl radicals and produced products with m/z values of 336 and 301. The imino groups were oxidized to aniline, which could further oxidize to nitrate anions. Peaks at m/z 279 and 267/ were observed for the hydroxylated products. Repeated hydroxylation opened aromatic rings of MB, and the corresponding peaks with m/z values of 214, 184,190, 125, and 109 were found in the spectra. Subsequently, aliphatic compounds with m/z values of 171, 156, 148, 142,130, and 102 were produced because of continuous hydroxylation. Finally, as a result of the ongoing reactions between the aliphatics and other reactive species in the system, they gradually mineralize. The existence of peaks at lower m/z ratios indicated that the dye molecule was successfully broken down into smaller pieces toward total deterioration. In addition, discoloration of the MB solution after the reaction is another way to recognize that the reaction catalyzed by the synthesized catalyst proceeds via dye degradation.

3.9. Toxicity Predictions of MB Solution during the Degradation Process. The toxicity of MB and its deterioration products under VL exposure for 60 min was studied through the ECOSAR program using the NZO/CNT composites. Table 1 and Figure S5 illustrate the assessment of acute (LC/EC$_{50}$) and chronic (ChV) toxicities of MB and its degradation intermediates. Three different aquatic organisms (fish, daphnia, and green algae) were chosen as the evaluation objects. Three toxicity levels were used to categorize the levels of toxicity: toxic (0 < toxicity values < 10 mg L^{-1}), harmful (10 < toxicity values < 100 mg L^{-1}), and not harmful (toxicity values > 100 mg L^{-1}). According to the calculations, the acute toxicity value of MB was 5.72 mg L^{-1} EC$_{50}$ for green algae, 3.88 mg L^{-1} LC$_{50}$ for daphnia, and 5.79 mg L^{-1} LC$_{50}$ for fish. According to these findings, MB is toxic to all three aquatic species (daphnia, green algae, and fish). The calculated chronic toxicity of MB to fish as ChV was 0.688 mg L^{-1}, and MB was chronically toxic to fish. However, after treatment with NZO/CNT under VL, the toxicity of the MB-contaminated water significantly decreased. The product m/z values of 284, 336, 301, 279, 267, 214, 190, 184, 171, 156, 148, 142, 130, 125, 109, and 102 are given the names MB, P1, P2, P3, P4, P5, P6, P7, P8, P9, P10, P11, P12, P13, P14, and P15, respectively. None of the deteriorated substances in the MB products showed any negative effects (toxic or harmful) on fish, daphnia, and green algae. Most of the products in the acute toxicity diagram for fish are harmless. Few products were found to be harmful compared with MB, and their toxicity was significantly reduced. No products were detected in the toxicity zone. Therefore, these results demonstrate that the photocatalytic process over VL using the synthesized NZO/CNT composites is tremendously efficient in detoxifying MB and is environmentally safe.

4. CONCLUSIONS

In summary, a novel NZO/CNT photocatalyst was successfully prepared via a simple step-by-step chemical synthesis process, followed by a cocrystallization approach. According to the characterization investigations, N was effectively doped into the ZnO matrix, and the CNTs were attached to the NZO surface without changing the rod-shaped structure of the ZnO lattice. The E_g value of undoped ZnO was significantly reduced

https://doi.org/10.1021/acsomega.3c00370
ACS Omega 2023, 8, 16174−16185

by the addition of N and CNT, and the e^-−h^+ pair recombination decreased. The photocatalytic efficiencies of the as-synthesized NZO/CNT composite were 92, 52, and 27% higher than those of photolysis, ZnO, and NZO, respectively. The photodegradation of MB proceeded according to pseudo-first-order reaction kinetics, and the rate constant values of NZO/CNT were 43.55, 5.35, and 2.74 times larger than those of photolysis, ZnO, and NZO, respectively. The photocatalytic efficiency and rate constant of NZO/CNT were considerably enhanced compared with those of the individual components (ZnO and NZO). Improved catalytic activity was achieved owing to the participation of N and CNT during the NZO/CNT composite formation. In addition, the NZO/CNT composite exhibits enhanced photocatalytic activity under basic conditions according to the pH_{PZC} investigation. The NZO/CNT photocatalyst demonstrated outstanding sustainability and recyclability after four consecutive runs, which were verified by using XRD and XPS. Furthermore, MB dye decomposition was analyzed using the as-prepared NZO/CNT, and possible degradation products were proposed. Subsequently, the toxicity of the decomposition products was estimated, which revealed that the degradation process was safe for the environment. Therefore, this study improves the process for removing noxious contaminants from wastewater, in addition to offering a simple method for the manufacture of NZO with CNT nanocomposites.

■ ASSOCIATED CONTENT

Supporting Information

The Supporting Information is available free of charge at https://pubs.acs.org/doi/10.1021/acsomega.3c00370.

XPS survey spectrum of the NZO/CNT compound; FE-SEM images of ZnO and NZO and ESD spectra of ZnO and NZO; before and after photocatalytic treatment under VL using NZO/CNT: XRD and XPS; plausible photodegradation products of MB; acute and chronic toxicity evaluation of MB and its photodegradation intermediates toward four aquatic organisms such as fish (LC_{50}), daphnia, green algae, and fish (ChV); rate constant (k, min^{-1}) for the degradation of MB dye along with R^2 values of all the inspected samples; and comparative studies of ZnO- or CNT-based composites for the degradation of various contaminants (PDF)

■ AUTHOR INFORMATION

Corresponding Authors

Md. Abu Hanif − *Institute of Carbon Technology, Jeonju University, Jeonju 55069, Korea;* orcid.org/0000-0002-2966-2484; Email: hanif21@jj.ac.kr

Lee Ku Kwac − *Institute of Carbon Technology, Jeonju University, Jeonju 55069, Korea; Graduate School of Carbon Convergence Engineering, Jeonju University, Jeonju 55069, Korea*; Email: kwac29@jj.ac.kr

Authors

Young-Soon Kim − *Institute of Carbon Technology, Jeonju University, Jeonju 55069, Korea;* orcid.org/0000-0001-8549-5951

Jeasmin Akter − *Department of Chemistry, Khulna University of Engineering & Technology, Khulna 9203, Bangladesh;* orcid.org/0000-0001-8858-6488

Hong Gun Kim − *Institute of Carbon Technology, Jeonju University, Jeonju 55069, Korea; Graduate School of Carbon Convergence Engineering, Jeonju University, Jeonju 55069, Korea*

Complete contact information is available at: https://pubs.acs.org/10.1021/acsomega.3c00370

Notes

The authors declare no competing financial interest.

■ ACKNOWLEDGMENTS

This research was supported by the Basic Science Research Program through the National Research Foundation of Korea (NRF), funded by the Ministry of Education (2016R1A6A1A03012069, 2018R1D1A1B07050752, and 2020R1A2C1102174).

■ REFERENCES

(1) Okesola, B. O.; Smith, D. K. Applying low-molecular weight supramolecular gelators in an environmental setting—self-assembled gels as smart materials for pollutant removal. *Chem. Soc. Rev.* **2016**, *45*, 4226−4251.

(2) Zhao, Y.; Ikram, M.; Zhang, J.; Kan, K.; Wu, H.; Song, W.; Li, L.; Shi, K. Outstanding gas sensing performance of CuO-CNTs nanocomposite based on asymmetrical schottky junctions. *Appl. Surf. Sci.* **2018**, *428*, 415−421.

(3) Abu Hanif, M.; Akter, J.; Akherul Islam, M.; Sapkota, K. P.; Hahn, J. R. Visible-light-driven enhanced photocatalytic performance using cadmium-doping of tungsten (VI) oxide and nanocomposite formation with graphitic carbon nitride disks. *Appl. Surf. Sci.* **2021**, *565*, 150541.

(4) Akter, J.; Hanif, M. A.; Islam, M. A.; Sapkota, K. P.; Lee, I.; Hahn, J. R. Visible-light-active novel α-Fe_2O_3/Ta_3N_5 photocatalyst designed by band-edge tuning and interfacial charge transfer for effective treatment of hazardous pollutants. *J. Environ. Chem. Eng.* **2021**, *9*, 106831.

(5) Kitchamsetti, N.; Ramteke, M. S.; Rondiya, S. R.; Mulani, S. R.; Patil, M. S.; Cross, R. W.; Dzade, N. Y.; Devan, R. S. DFT and experimental investigations on the photocatalytic activities of NiO nanobelts for removal of organic pollutants. *J. Alloys Compd.* **2021**, *855*, 157337.

(6) Akter, J.; Hanif, M. A.; Islam, M. A.; Sapkota, K. P.; Hahn, J. R. Selective growth of Ti^{3+}/TiO_2/CNT and Ti^{3+}/TiO_2/C nanocomposite for enhanced visible-light utilization to degrade organic pollutants by lowering TiO^2-bandgap. *Sci. Rep.* **2021**, *11*, 9490.

(7) Sudrajat, H.; Babel, S. A novel visible light active N-doped ZnO for photocatalytic degradation of dyes. *J. Water Process. Eng.* **2017**, *16*, 309−318.

(8) Han, Z. Z.; Liao, L.; Wu, Y. T.; Pan, H. B.; Shen, S. F.; Chen, J. Z. Synthesis and photocatalytic application of oriented hierarchical ZnO flower-rod architectures. *J. Hazard. Mater.* **2012**, *217−218*, 100−106.

(9) Prathap Kumar, M.; Suganya Josephine, G.; Sivasamy, A. Oxidation of organic dye using nanocrystalline rare earth metal ion doped CeO_2 under UV and visible light irradiations. *J. Mol. Liq.* **2017**, *242*, 789−797.

(10) Zhang, Y. D.; Zheng, Z.; Yang, F. L. Highly sensitive and selective alcohol sensors based on Ag-doped In_2O_3 coating. *Ind. Eng. Chem. Res.* **2010**, *49*, 3539−3543.

(11) Vernardou, D.; Drosos, H.; Spanakis, E.; Koudoumas, E.; Savvakis, C.; Katsarakis, N. Electrochemical and photocatalytic properties of WO_3 coatings grown at low temperatures. *J. Mater. Chem.* **2011**, *21*, 513−517.

(12) Zhang, Y. R.; Wan, J.; Ke, Y. U. A novel approach of preparing TiO_2 films at low temperature and its application in photocatalytic degradation of methyl orange. *J. Hazard. Mater.* **2010**, *177*, 750−754.

(13) Alanazi, H. S.; Ahmad, N.; Alharthi, F. A. Synthesis of Gd/N co-doped ZnO for enhanced UV-vis and direct solar-light-driven photocatalytic degradation. *RSC Adv.* **2021**, *11*, 10194−10202.
(14) Abu Hanif, M.; Akter, J.; Akherul Islam, M.; Lee, I.; Prasad Sapkota, K.; Shrestha, S.; Pandey, A.; Gyawali, N.; Ryang Hahn, J. Enhancement of visible-light photocatalytic activity of ZnO/ZnS/g-C_3N_4 by decreasing the bandgap and reducing the crystallite size via facile one-step fabrication. *J. Photochem. Photobiol., A* **2022**, *431*, 114066.
(15) Dong, Z.; Wu, Y.; Thirugnanam, N.; Li, G. Double Z-scheme ZnO/ZnS/g-C_3N_4 ternary structure for efficient photocatalytic H_2 production. *Appl. Surf. Sci.* **2018**, *430*, 293−300.
(16) Azqhandi, M. H. A.; Vasheghani, F. B.; Rajabi, F. H.; Keramati, M. Synthesis of Cd doped ZnO/CNT nanocomposite by using microwave method: Photocatalytic behavior, adsorption, and kinetic study. *Results Phys.* **2017**, *7*, 1106−1114.
(17) Li, D.; Haneda, H. Synthesis of nitrogen-containing ZnO powders by spray pyrolysis and their visible-light photocatalysis in gas-phase acetaldehyde decomposition. *J. Photochem. Photobiol., A* **2003**, *155*, 171−178.
(18) Qin, H.; Li, W.; Xia, Y.; He, T. Photocatalytic activity of heterostructures based on ZnO and N-doped ZnO. *ACS Appl. Mater. Interfaces* **2011**, *3*, 3152−3156.
(19) Lu, J.; Zhang, Q.; Wang, J.; Saito, F.; Uchida, M. Synthesis of N-Doped ZnO by grinding and subsequent heating ZnO-urea mixture. *Powder Technol.* **2006**, *162*, 33−37.
(20) Duclère, J.-R.; Novotny, M.; Meaney, A.; O'Haire, R.; McGlynn, E.; Henry, M.; Mosnier, J.-P. Properties of Li-P-and N-doped ZnO thin films prepared by pulsed laser deposition. *Superlattices Microstruct.* **2005**, *38*, 397−405.
(21) Zhao, J.-L.; Li, X.-M.; Bian, J.-M.; Yu, W.-D.; Zhang, C.-Y. Growth of nitrogen-doped p-type ZnO films by spray pyrolysis and their electrical and optical properties. *J. Cryst. Growth* **2005**, *280*, 495−501.
(22) Nakano, Y.; Morikawa, T.; Ohwaki, T.; Taga, Y. Deep-level characterization of N-doped ZnO films prepared by reactive magnetron sputtering. *Appl. Phys. Lett.* **2005**, *87*, 232104.
(23) Perkins, C. L.; Lee, S.-H.; Li, X.; Asher, S. E.; Coutts, T. J. Identification of nitrogen chemical states in N-doped ZnO via x-ray photoelectron spectroscopy. *J. Appl. Phys.* **2005**, *97*, 034907.
(24) Gautam, U. K.; Panchakarla, L.; Dierre, B.; Fang, X.; Bando, Y.; Sekiguchi, T.; Govindaraj, A.; Golberg, D.; Rao, C. Solvothermal synthesis, cathodoluminescence, and field- emission properties of pure and N- doped ZnO nanobullets. *Adv. Funct. Mater.* **2009**, *19*, 131−140.
(25) Bhirud, A. P.; Sathaye, S. D.; Waichal, R. P.; Nikam, L. K.; Kale, B. B. An eco-friendly, highly stable and efficient nanostructured p-type N-doped ZnO photocatalyst for environmentally benign solar hydrogen production. *Green Chem.* **2012**, *14*, 2790−2798.
(26) Elashmawi, I. S.; H Gaabour, L. H. Raman, morphology and electrical behavior of nanocomposites based on PEO/PVDF with multi-walled carbon nanotubes. *Results Phys.* **2015**, *5*, 105−110.
(27) Salar Elahi, A.; Agah, K. M.; Ghoranneviss, M. A new perspective on structural and morphological properties of carbon nanotubes synthesized by plasma enhanced chemical vapor deposition technique. *Results Phys.* **2017**, *7*, 757−761.
(28) Hanif, M. A.; Kim, Y. S.; Ameen, S.; Kim, H. G.; Kwac, L. K. Boosting the Visible Light Photocatalytic Activity of ZnO through the Incorporation of N-Doped for Wastewater Treatment. *Coatings* **2022**, *12*, 579.
(29) Hanif, M. A.; Akter, J.; Lee, I.; Islam, M. A.; Sapkota, K. P.; Abbas, H. G.; Hahn, J. R. Formation of chemical heterojunctions between ZnO nanoparticles and single-walled carbon nanotubes for synergistic enhancement of photocatalytic activity. *J. Photochem. Photobiol., A* **2021**, *413*, 113260.
(30) Xiao, X.; Han, B.; Chen, G.; Wang, L.; Wang, Y. Preparation and electrochemical performances of carbon sphere@ZnO core-shell nanocomposite for supercapacitor applications. *Sci. Rep.* **2017**, *7*, 40167.
(31) Yang, X. Y.; Wolcott, A.; Wang, G. M.; Sobo, A.; Fitzmorris, R. C.; Qian, F.; Zhang, J. Z.; Li, Y. Nitrogen-Doped ZnO Nanowire Arrays for Photoelectrochemical Water Splitting. *Nano Lett.* **2009**, *9*, 2331−2336.
(32) De Menezes, B. R. C.; Ferreira, F. V.; Silva, B. C.; Simonetti, E. A. N.; Bastos, T. M.; Cividanes, L. S.; Thim, G. P. Effects of Octadecylamine Functionalization of Carbon Nanotubes on Dispersion, Polarity, and Mechanical Properties of CNT/HDPE Nanocomposites. *J. Mater. Sci.* **2018**, *53*, 14311−14327.
(33) Buryi, M.; Remeš, Z.; Babin, V.; Novotný, M.; Vaněček, V.; Aubrechtová Dragounová, K.; Mičová, J.; Landová, L.; Kučerková, R.; MoreChevalier, J.; Chertopalov, S.; Fitl, P.; Kmječ, T. Influence of Mo doping on the luminescence properties and defect states in ZnO nanorods. Comparison with ZnO: Mo thin films. *Appl. Surf. Sci.* **2021**, *555*, 149679.
(34) Li, J.; Dai, Z.; Li, H. Controllable Mn-doped ZnO nanorods for direct assembly of a photoelectrochemical aptasensor. *Analyst* **2017**, *142*, 2177−2184.
(35) Hou, C. T.; Liu, W. L. One-step synthesis of OH-TiO_2/$TiOF_2$ nanohybrids and their enhanced solar light photocatalytic performance. *R. Soc. Open Sci.* **2018**, *5*, 172005.
(36) De la Flor, M. P.; Camarillo, R.; Martínez, F.; Jiménez, C.; Quiles, R.; Rincón, J. Removal of emerging pollutant dibutylhydroxytoluene from water with CNT/TiO_2 catalysts in a visible LED photoreactor. *Environ. Sci. Pollut. Res.* **2021**, *28*, 23720−23730.
(37) Yao, Y.; Li, G.; Ciston, S.; Lueptow, R. M.; Gray, K. A. Photoreactive TiO_2/carbon nanotube composites: synthesis and reactivity. *Environ. Sci. Technol.* **2008**, *42*, 4952−4957.
(38) Dai, K.; Zhang, X.; Fan, K.; Peng, T.; Wei, B. Hydrothermal synthesis of single-walled carbon nanotube−TiO_2 hybrid and its photocatalytic activity. *Appl. Surf. Sci.* **2013**, *270*, 238−244.
(39) Ling, L.; Wang, C.; Ni, M.; Shang, C. Enhanced photocatalytic activity of TiO_2/single-walled carbon nanotube (SWCNT) composites under UV-A irradiation. *Sep. Purif. Technol.* **2016**, *169*, 273−278.
(40) Woan, K.; Pyrgiotakis, G.; Sigmund, W. Photocatalytic carbon-nanotube TiO_2 composites. *Adv. Mater.* **2009**, *21*, 2233−2239.
(41) Yi, Q.; Wang, H.; Cong, S.; Cao, Y.; Wang, Y.; Sun, Y.; Lou, Y.; Zhao, J.; Wu, J.; Zou, G. Self-cleaning glass of photocatalytic anatase TiO_2@carbon nanotubes thin film by polymer-assisted approach. *Nanoscale Res. Lett.* **2016**, *11*, 457.

https://doi.org/10.1021/acsomega.3c00370
ACS Omega 2023, 8, 16174−16185